Acoustic helical dichroism in a one-dimensional lattice of chiral resonators

Qing Tong◉ and Shubo Wang◉*

Department of Physics, City University of Hong Kong, Tat Chee Avenue, Kowloon, Hong Kong, China

Circular dichroism and helical dichroism are intriguing chiroptical phenomena with broad applications in optical sensing and imaging. Here, we generalize one of the phenomena-helical dichroism-to acoustics. We show that a one-dimensional lattice of chiral resonators with loss can induce differential absorption of helical sounds (i.e., acoustic vortices) carrying opposite orbital angular momentum (OAM). This acoustic helical dichroism strongly depends on the rotation symmetry of the chiral resonators. Breaking the C_4 rotation symmetry can induce coupling between the opposite chiral dipole modes of the resonators. This leads to OAM band gaps and non-Hermitian exceptional points near the Brillouin-zone center and boundaries, which together give rise to significantly enhanced helical dichroism. The underlying physics can be well captured by an effective Hamiltonian that quantitatively reproduces the complex band structures. The acoustic helical dichroism can find important applications in acoustic OAM manipulations and chiral sound-matter interactions.

I. INTRODUCTION

Chiroptical effects induced by the interaction of light with chiral structures have attracted considerable interest due to broad applications in physics, chemistry, and biology [1–5]. One intriguing chiroptical effect is circular dichroism (CD), i.e., the differential absorption of right-handed circularly polarized and left-handed circularly polarized lights [6]. It has been widely used to detect and analyze chiral structures, including proteins [7], DNA, and pharmaceutical drugs [8], and liquid crystals [9], as well as to control rotatory power [10]. However, chiral optical interactions in nature are usually very weak due to a significant size mismatch between the chiral structures and light's wavelength [5]. Therefore, various artificial structures have been proposed to achieve strong CD effects, including chiral metamaterials [10–14], chiral metasurfaces [15], and gyroid structures [16–18]. Interestingly, a strong CD effect can also be realized by using an achiral metal sphere excited by a linearly polarized light [19]. Akin to CD, optical vortex beams (i.e., helical lights) carrying opposite orbital angular momentum (OAM) can also manifest different absorptions when interacting with chiral structures, which is referred to as optical helical dichroism (HD) [5]. In contrast to CD resulting from the coupling between electric and magnetic dipoles [20], HD is attributed to the electric quadrupole moments induced by the interaction of optical OAM with chiral structures [21], which has been verified theoretically [22–25] and experimentally [26,27].

Despite the extensive study of CD and HD effects in optics, the exploration of their counterparts in acoustics has not been reported yet. Sound propagating in air/fluids is a longitudinal wave carrying no intrinsic spin angular momentum [28,29], indicating the absence of an acoustic analog of optical CD. However, sound can carry intrinsic OAM in the form of acoustic vortex beams (i.e., helical sounds) characterized by a topological charge q [30–36], which can give rise to many novel phenomena and applications similar to optical OAM, such as acoustic micromanipulations [37,38], acoustic communications via OAM multiplexing [39], acoustic spin-redirection geometric phase [40], and acoustic Fedorov-Imbert linear shift [41]. An interesting question is whether sound can have the phenomenon of HD. In this paper, we report that a one-dimensional (1D) periodical lattice of chiral resonators can induce differential absorption of opposite helical sounds (i.e., helical sounds carrying opposite OAM), which we refer to as acoustic HD. This phenomenon is attributed to the interaction of acoustic OAM with the chiral resonators. We show that the chiral resonators with homogenous loss respecting C_4 rotation symmetry induce weak acoustic HD. To achieve a large HD, we engineer the loss region to break the C_4 rotation symmetry and induce the coupling of opposite chiral dipole states of the resonators. This gives rise to OAM band gaps and non-Hermitian exceptional points (EPs), which can significantly enhance the acoustic HD. We show that the underlying physics can be well captured by an effective Hamiltonian taking into account the chiral dipole bands of the 1D lattice. These results provide new mechanisms to manipulate acoustic OAM (e.g., selective absorption or transmission of acoustic OAM) and can trigger more explorations of acoustic chiral-matter interactions.

We organize the paper as follows. In Sec. II, we describe the 1D lattice of chiral resonators and the properties of the band structures and eigenmodes. In Sec. III, we discuss the acoustic HD effect in two types of lossy lattice with C_4 and C_2 symmetry, respectively, where the symmetry is determined by the loss region. The physics for the HD effect is illustrated in Sec. IV using an effective Hamiltonian that can reproduce the band structures of the C_4 and C_2 systems. To further verify our theory, in Sec. V, we consider another type of lattice with C_2 symmetry determined by the unit cell's geometry. We draw the conclusion in Sec. VI.

*Corresponding author: shubwang@cityu.edu.hk
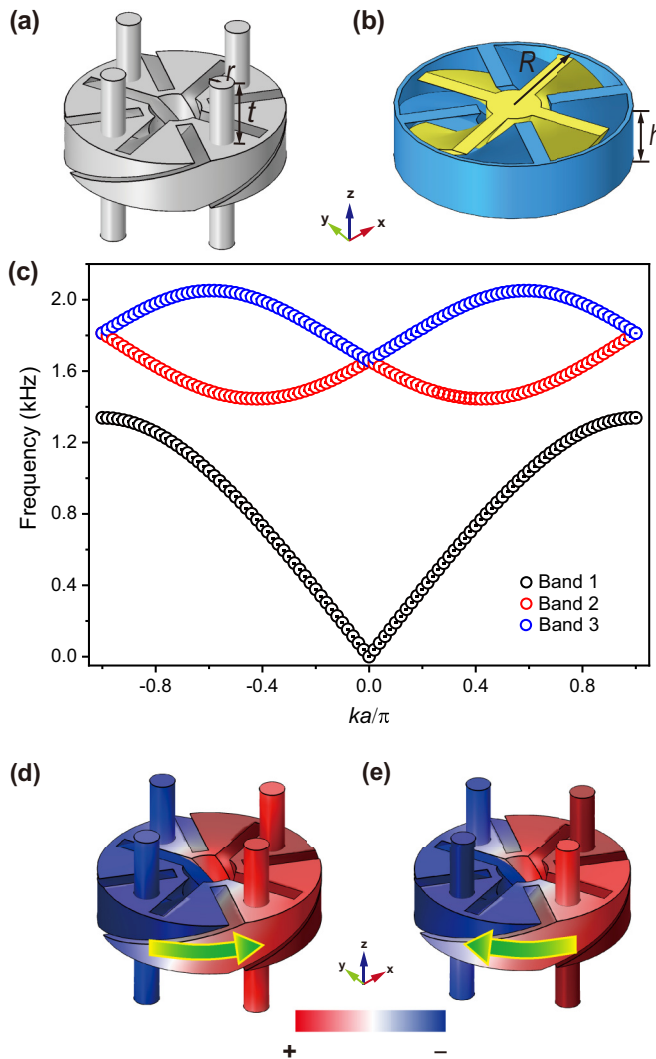
FIG. 1. (a) Unit cell of the 1D chiral lattice. (b) A cutaway view of the chiral resonator. The inner blades are colored in yellow. The outer blades and the shell are colored in blue. The geometric parameters are $r = 0.285$ cm, $t = 1.5$ cm, $R = 2.5$ cm, and $h = 1.25$ cm. (c) Band structure of the 1D chiral lattice. The eigenpressure fields of the second and third bands at $ka/\pi = 0.2$ are shown in (d) and (e), respectively. The green arrows indicate the rotation direction of the pressure fields.

II. 1D LATTICE OF CHIRAL RESONATORS

We consider a 1D periodical structure along the z direction with the unit cell shown in Figs. 1(a) and 1(b). The unit cell consists of a right-handed chiral resonator (filled with air) with eight tubes that introduce coupling between nearby unit cells. Figure 1(a) shows the air domain of the unit cell. Figure 1(b) shows a cutaway view of the solid shell and blades of the chiral resonator (the solid shells of the tubes are not shown), where the internal (yellow) and external (blue) blades segment the air inside the resonator. We assume hard boundary conditions at all solid-air interfaces. Such an internal structure of the resonator enables subwavelength resonances via space coiling. The blades are twisted by $\pi/2$ to introduce chirality into the resonator that breaks the inversion symmetry. The

cylindrical resonator has a radius of $R = 2.5$ cm and a height of $h = 1.25$ cm. The tubes have radii of $r = 0.285$ cm and a height of $t = 1.5$ cm.

We conducted full-wave simulations of the periodic structure and computed its band structures using a finite-element package COMSOL MULTIPHYSICS [42]. The results are shown in Fig. 1(c) for the lowest three bands, where k is the magnitude of the wave vector along the z direction, and $a = 2t + h$ is the lattice period. The first band extending to the static limit corresponds to a monopole mode that has a constant phase of pressure inside the resonator at $k = 0$. The second and third bands correspond to two chiral dipole modes carrying opposite OAM. The two bands are degenerate at $k = 0$ as a result of the C_4 rotation symmetry. At $k \neq 0$, the two bands have split due to the inversion symmetry breaking of the chiral resonator. Figures 1(d) and 1(e) show the eigenpressure fields of the opposite chiral dipole modes at $ka/\pi = 0.2$. The blue and red colors denote negative and positive pressures, respectively. The green arrows show the circulating directions of the pressure field as time elapses. Clearly, the modes are of dipole nature and have opposite chirality, i.e., they carry opposite OAM. Importantly, the dipole modes are transverse (perpendicular to the propagating direction) and give rise to a transverse sound. The rotation of the pressure fields can be realized by selectively exciting the chiral dipole modes using four input ports with proper phases (see the details in Sec. III). In the following, we will focus on the interaction of helical sounds with the chiral lattice at the frequencies of the dipole modes and characterize their different absorption properties.

III. ACOUSTIC HELICAL DICHROISM

To demonstrate the phenomenon of acoustic HD, we consider the 1D lattice consisting of ten unit cells shown in Fig. 2(a). We excite the structure via the tubes on the left side of the lattice and calculate the power transmission and reflection coefficients by using COMSOL. For helical sound with topological charge $q = +1$, the incident pressure at the four input tubes has a phase of $0, 0.5\pi, \pi$, and 1.5π in the azimuthal direction. For helical sound with a topological charge $q = -1$, the above phases take an extra minus sign. To achieve sound absorption, we introduce loss into the resonators by adding an imaginary part to the speed of sound as $v(1 + i\alpha)$, where v is the speed of sound in air and α characterizes the loss strength. Let us denote the reflection and transmission of power as $R_{\pm}$ and $T_{\pm}$, respectively, where "$\pm$" denotes the sign of the topological charge q carried by the input helical sounds. Then, the absorption for sound with $q = \pm 1$ and the differential absorption characterizing the acoustic HD can be determined as

$$A_{\pm} = 1 - R_{\pm} - T_{\pm}, \tag{1}$$

$$\Delta A = |A_+ - A_-|. \tag{2}$$

We first consider the case with homogeneous loss introduced into the chiral resonators, as shown by the inset in Fig. 2(b), where the blue region of the resonator contains loss. The C_4 rotation symmetry is still maintained in this case. The numerical simulation results for the reflection and transmission coefficients are shown as solid and dashed lines in
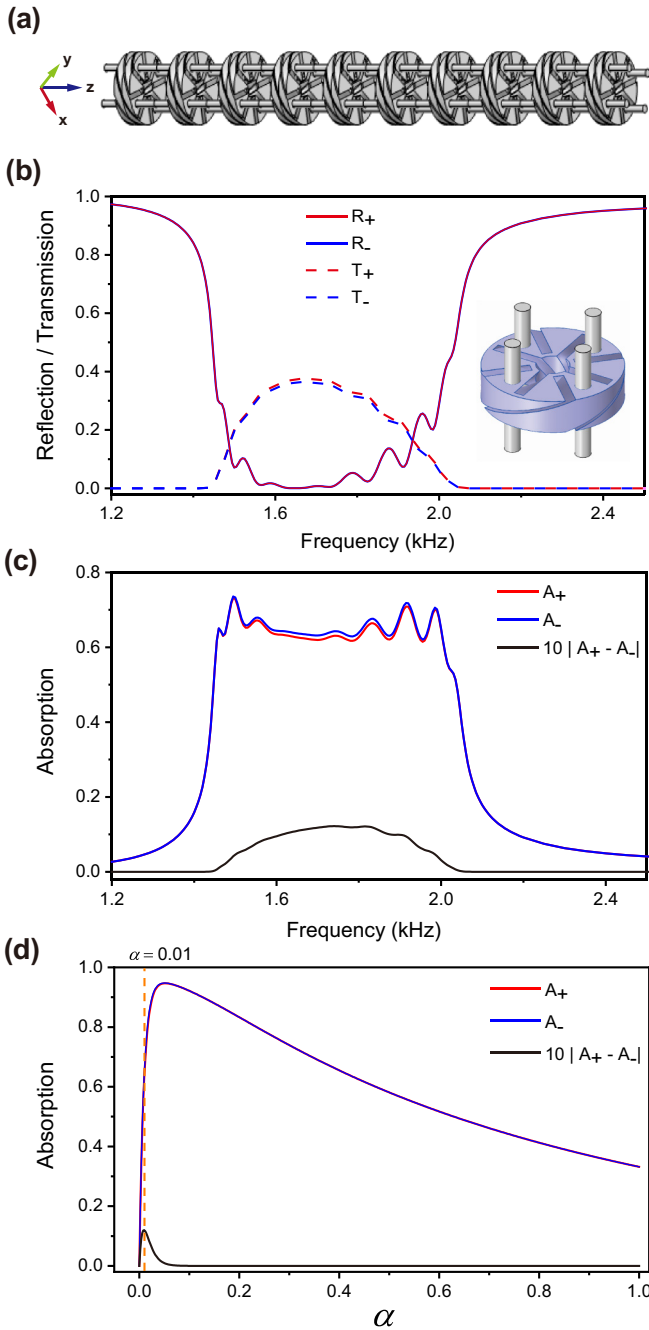
FIG. 2. (a) The 1D chiral lattice consisting of ten unit cells. (b) Transmissions, reflections, and (c) absorptions of helical sounds carrying opposite OAM. The loss is homogeneously added to all the resonators, and the loss parameters $\alpha = 0.01$. (d) Absorptions of opposite helical sounds as a function of loss parameters α at $f = 1.8$ kHz. The differential loss is multiplied by ten.

Fig. 2(b). We have set the loss parameters $\alpha = 0.01$. As seen, the reflections of opposite helical sounds, i.e., R_+ and R_-, are almost identical, while the transmissions T_+ and T_- are slightly different. The absorption coefficients obtained using Eq. (1) are shown in Fig. 2(c) as solid blue and red lines. We see that the absorptions of opposite helical sounds have small differences within the frequency range (1.45 kHz, 2.04 kHz), corresponding to the frequencies of the chiral dipole bands in

Fig. 1(c). The solid black line shows the differential absorption multiplied by ten, i.e., $\Delta A \times 10$. To understand whether the weak HD is attributed to the small loss parameter $\alpha = 0.01$, we calculated the absorption at the frequency of 1.8 kHz while varying the value of α, and the results are shown in Fig. 2(d). We see that, as α is enlarged, the absorptions of opposite helical sounds first increase and then decrease. The same trend is also found for the differential absorption, which has a maximum value $\Delta A \approx 0.01$ at $\alpha = 0.01$ (marked by the dashed yellow line). Therefore, this lossy lattice with C_4 symmetry cannot induce large HD.

We now consider the lattice with inhomogeneous loss introduced into the chiral resonators, as shown by the inset in Fig. 3(a), where only two sections (blued) of the chiral resonator contain loss. The unit cell now possesses C_2 rotation symmetry. We simulated the transmission and reflection of the lattice for helical sounds with topological charge $q = \pm 1$, and the results are shown in Fig. 3(a) as the solid and dashed lines, where the loss parameter is $\alpha = 0.22$. We see that both the transmission and reflection of $q = +1$ helical sound have a resonance peak at $f = 1.81$ kHz, while the transmission and reflection of $q = -1$ helical sound have a resonance peak at $f = 1.66$ kHz. These peaks lead to a large acoustic HD, as shown in Fig. 3(b) by the solid black line. Remarkably, the HD can reach about 40% at the resonance frequencies. The solid blue and red lines denote the absorption $A_\pm$ obtained using Eq. (1), which shows a dip at corresponding resonance frequencies. We also calculated the absorption as a function of loss strength α at the fixed frequency $f = 1.8$ kHz, and the results are shown in Fig. 3(c). Similar to the C_4 system, as α is enlarged, the absorptions of the helical sounds first increase and then decrease. A similar feature is also observed for the differential loss ΔA. The maximum value of ΔA appears at $\alpha = 0.22$, which is the value we set for computing the results in Figs. 3(a) and 3(b). Apparently, the acoustic HD in this C_2 system is much stronger than that of the C_4 system in Fig. 2. We will show that the strong acoustic HD can be attributed to the combined effect of OAM band gaps and non-Hermitian EPs. The different values of T_+ and T_- in Fig. 3(a) suggest that the chiral lattice can be employed to generate helical sound with achiral excitation. As a demonstration, we excite the lattice by setting the phase of the pressure at four input tubes to be 0, 0, π, and π, respectively, corresponding to a "linearly" polarized input sound. The amplitude and phase of the transmitted pressure at $f = 1.81$ kHz are shown in Figs. 3(d) and 3(e). We notice that the pressure amplitude has an approximate doughnut shape with zero value in the center, and the phase pattern shows a 2π variation in the azimuthal direction. These confirm the generation of $q = +1$ helical sound in the transmitted field. The distortion of amplitude donut is attributed to the residue sound with $q = -1$. We note that similar property also exists in the reflected sound, as indicated by the different values of R_+ and R_- at the frequencies of the dipole bands in Fig. 3(a).

IV. COMPLEX BAND STRUCTURES AND EXCEPTIONAL POINTS

To understand the underlying physics of the acoustic HD, we study the complex band structures of the 1D lattice with
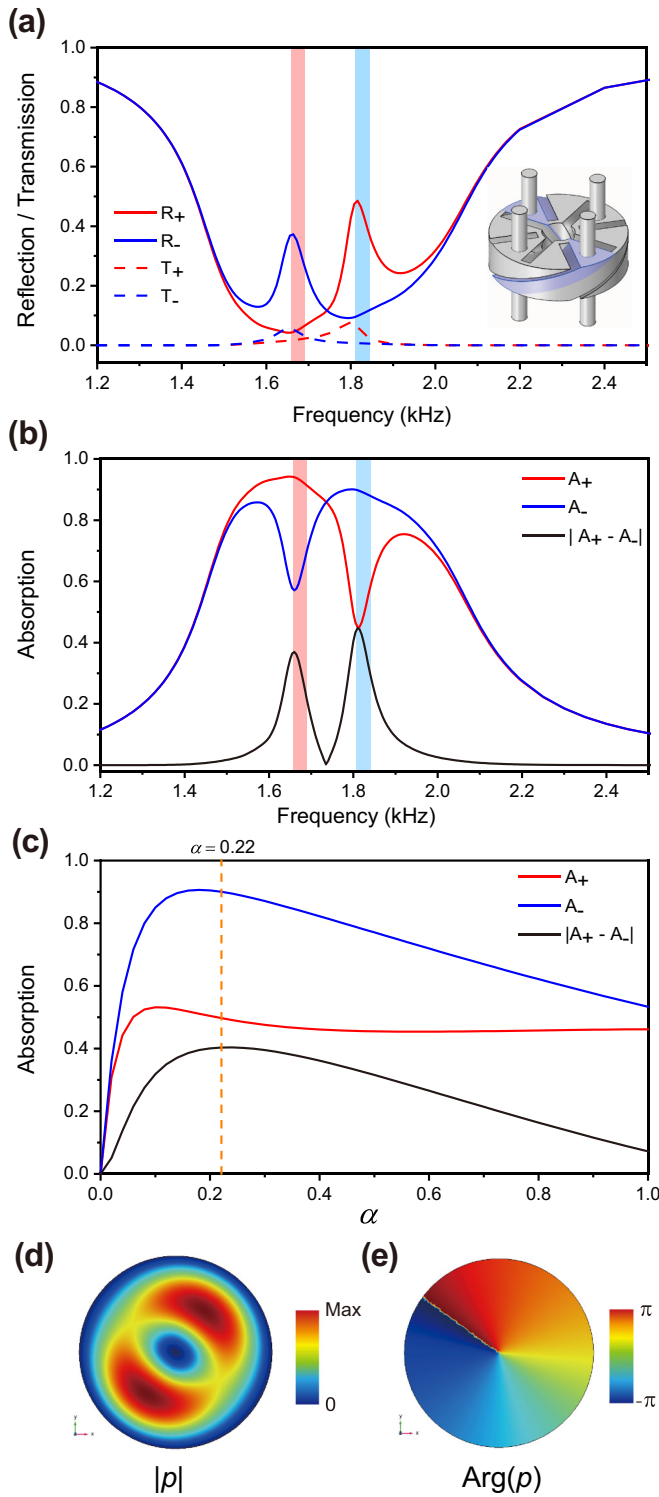
FIG. 3. (a) Transmissions, reflections, and (b) absorptions of helical sounds carrying opposite OAM. The loss is selectively added to two opposing sections of the chiral resonators, and we set $\alpha = 0.22$. The red and blue ribbons mark the OAM gaps (see main text for definition). (c) Absorption of opposite helical sounds as a function of the loss parameter α at $f = 1.8$ kHz. (d) The amplitude and (e) phase of output pressure field under the excitation of a "linearly" polarized input sound for $\alpha = 0.22$ and $f = 1.82$ kHz.
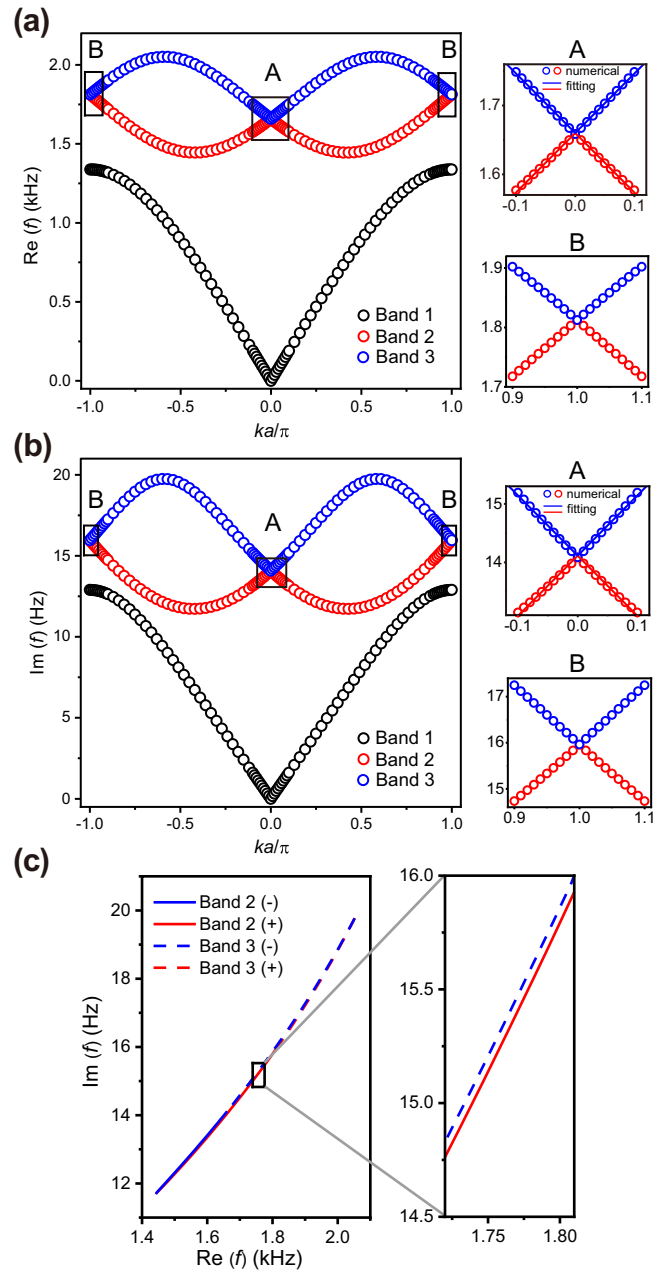
FIG. 4. (a) The real part and (b) the imaginary part of the complex band structure for the C_4 system with $\alpha = 0.01$. The right insets show the zoom-ins of the bands near the zone center and boundaries, as indicated by the black rectangles in (a) and (b). (c) Eigenfrequencies corresponding to the second and third bands plotted in the complex plane. The red (blue) color denotes eigenstates with positive (negative) OAM. The right inset is a zoom-in showing the difference of the eigenfrequencies.

damping. We first consider the lossy lattice with C_4 symmetry corresponding to the case of Fig. 3. The numerically computed complex band structures for $\alpha = 0.01$ are shown in Figs. 4(a) and 4(b), respectively. We notice that the real and imaginary parts of eigenfrequencies have a similar structure. The imaginary parts are positive because of the time-harmonic convention $e^{i\omega t}$ adopted in numerical simulations. The right insets (labeled as A and B) show the zoom-ins of the bands
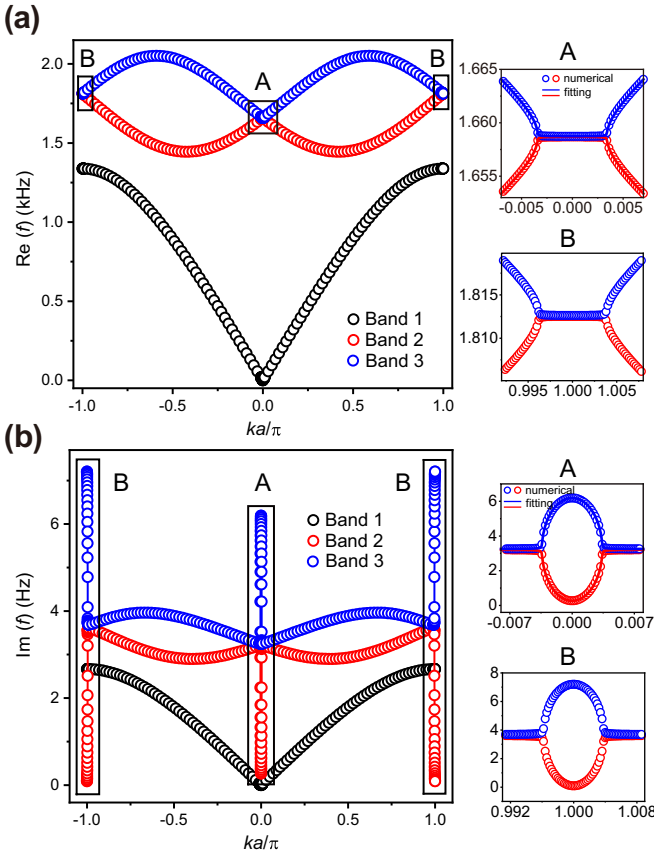
FIG. 5. (a) The real part and (b) the imaginary part of the complex band structure for the C_2 system with $\alpha = 0.01$. The right insets show the zoom-ins of the bands near the zone center and boundaries, as indicated by the black rectangles in (a) and (b).

near the zone center and boundaries, as marked by the black rectangles inset B corresponds to the composition of two zoom-in regions in Fig. 4(a)]. We see that both the real and imaginary parts are degenerate at the zone center and boundaries, which is protected by the C_4 rotation symmetry of the lattice and indicates vanished coupling between the opposite chiral dipole modes.

To understand the weak HD in Fig. 2, we plot the eigenfrequencies of the second and third bands in the complex plane, as shown in Fig. 4(c). The solid (dashed) lines correspond to the second (third) band. The red (blue) color denotes a positive (negative) OAM carried by the corresponding eigenstates (i.e., chiral dipole modes), as labeled by a "+" ("−") sign in the figure legend. We notice that the OAM carried by the eigenstates of each band can change the sign because the group and phase velocities can change their relative sign [29]. The right inset in Fig. 4(c) shows a zoom-in of the complex eigenfrequencies, from which we observe a small separation between the red and blue lines. Therefore, under the excitation of input helical sounds within this frequency range, the chiral dipole modes with opposite OAM have different damping. This gives rise to the differential absorption of input helical sounds with opposite OAM, i.e., the acoustic HD.

We now consider the lossy lattice with C_2 rotation symmetry shown in Fig. 3(a). Figure 5 shows the numerically

computed complex band structures for $\alpha = 0.01$. In contrast to the C_4 system, there are two EPs appearing at the zone center and another two EPs appearing at the zone boundaries. The right insets A and B in Figs. 5(a) and 5(b) show the zoom-ins of the real and imaginary parts of the bands near the EPs. We notice the typical bifurcation features of EPs: the real parts are degenerate in the symmetry-breaking phase while the imaginary parts bifurcate. These EPs can be considered as derived from the diabolic points in the original lossless system and thus are similar to the EPs emerged in coupled waveguides [43,44] or EPs spawning from a Dirac point in photonic crystals [45].

Figures 6(a) and 6(b) show the complex band structures of the C_2 system with a larger loss $\alpha = 0.22$, corresponding to the case of Figs. 3(a) and 3(b). We notice that the general structure of the bands is similar to that in Fig. 5. However, while the general features (e.g., bifurcations) of the EPs can still be observed, there are partial gaps that appear near the zone center and boundaries, making the EPs not well defined. The gaps associated with the real parts of the bands in Fig. 6(a) can be called OAM gaps since the lattice only allows the propagation of one chiral dipole mode within the gaps. Such OAM gaps are similar to the polarization gaps that have been well studied in optical chiral metamaterials [46]. We apply blue and red colors to label the two gaps in the insets A and B. The frequency ranges of these OAM gaps are also marked in Figs. 3(a) and 3(b). Noticeably, they agree with the peaks of the acoustic HD. To understand this agreement, we plot the eigenfrequencies of the dipole bands in the complex plane, as shown in Fig. 6(c). Similar to Fig. 4(c), we use red (blue) color to denote the eigenstates carrying positive (negative) OAM, as labeled by a symbol of "+" ("−") in the figure legend. We also marked the ranges of the two OAM gaps using blue and red ribbons. Remarkably, near the blue/red ribbon, the eigenfrequencies of opposite eigenstates have the largest differences in the imaginary parts, which is attributed to the combined effect of the EPs and the OAM gaps. This explains the large acoustic HD in the frequency ranges labeled by the blue and red ribbons in Fig. 3(b).

We now employ effective Hamiltonians to obtain a better understanding of the physics associated with the EPs [45,47–49]. For the homogeneous lossy lattice with C_4 symmetry, the effective Hamiltonian for the chiral dipole bands at $k \rightarrow 0$ can be expressed as

$$H_{C_4} = \begin{pmatrix} \omega_0 - i\gamma & (v_R + iv_I)k \\ (v_R + iv_I)k & \omega_0 - i\gamma \end{pmatrix} \qquad (3)$$

with complex eigenvalues:

$$\omega_{C_4} = \omega_0 - i\gamma \pm k(v_R + iv_I), \qquad (4)$$

where ω_0 is the eigenfrequency of the chiral dipole modes at $k = 0$ (corresponding to the degeneracy), v_R and v_I are the real and imaginary parts of the group velocity, k is the magnitude of the wave vector, and γ denotes the loss. As for the C_2 system, the effective Hamiltonian is

$$H_{C_2} = \begin{pmatrix} \omega_0 - i\gamma_1 + \frac{\delta}{2} & (v_R + iv_I)k \\ (v_R + iv_I)k & \omega_0 - i\gamma_2 - \frac{\delta}{2} \end{pmatrix} \qquad (5)$$
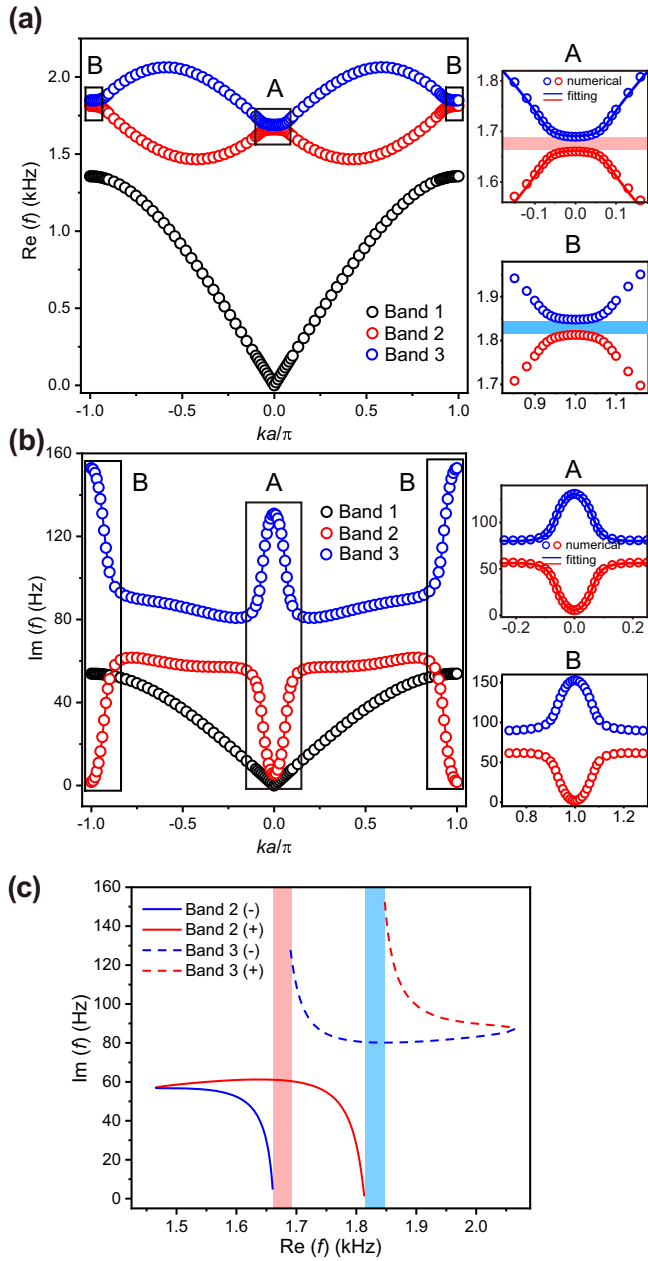
FIG. 6. (a) The real part and (b) the imaginary part of the complex band structure for the C_2 system with $\alpha = 0.22$. The right insets show the zoom-ins of the bands near the zone center and boundaries, as indicated by the black rectangles in (a) and (b). The red (blue) ribbon denotes the OAM gap where the helical sound with positive (negative) OAM can propagate inside the lattice. (c) Eigenfrequencies corresponding to the second and third bands plotted in the complex plane. The red (blue) color denotes eigenstates with positive (negative) OAM.

with complex eigenvalues:

$$\omega_{C_2} = \omega_0 - i\frac{(\gamma_1 + \gamma_2)}{2}$$
$$\pm \frac{1}{2}\sqrt{[\delta - i(\gamma_1 - \gamma_2)]^2 - 4k^2(v_I - iv_R)^2}, \quad (6)$$

where $\pm\delta/2$ describes the gap induced by the symmetry breaking and $\gamma_{1,2}$ denotes the loss of opposite chiral dipole modes at $k = 0$. Here, $\gamma_1 \neq \gamma_2$ due to the inhomogeneous loss added to the chiral resonator.

We apply Eqs. (4) and (6) to fit the numerically obtained complex band structures in the insets A of Figs. 4–6, from which we obtain the values for the parameters in the effective Hamiltonian. For the C_4 system in Figs. 4(a) and 4(b), the obtained parameters are $\gamma = -14.12$ Hz, $v_R = 11.71$ m/s, $v_I = 0.14$ m/s, and $\omega_0 = 1660.07$ Hz. For the C_2 system in Figs. 5(a) and 5(b), the obtained parameters are $\delta = 0.06$ Hz, $\gamma_1 = -6.19$ Hz, $\gamma_2 = -0.27$ Hz, $v_R = 11.81$ m/s, $v_I = 0.02$ m/s, and $\omega_0 = 1658.72$ Hz. For the C_2 system in Figs. 6(a) and 6(b), the obtained parameters are $\delta = 29.18$ Hz, $\gamma_1 = -130.81$ Hz, $\gamma_2 = -5.51$ Hz, $v_R = 11.76$ m/s, $v_I = 0.40$ m/s, and $\omega_0 = 1676.43$ Hz. Here, the loss parameters take negative values due to the time convention $e^{i\omega t}$ adopted in the numerical simulations. The analytical fitting results are shown as solid blue and red lines in the same insets. As seen, the analytical results given by the effective Hamiltonians well agree with the full-wave numerical results, demonstrating the validity of the effective Hamiltonians. The above analytical model provides a clear physical picture for the stronger acoustic HD in the C2 system. In the C_4 system with homogeneous loss, the eigenstates of the two bands at $k = 0$ are orthogonal and have no coupling. The dampings of the eigenstates with opposite OAM are approximately equal due to the homogeneous material loss. In the C_2 system with inhomogeneous material loss, the symmetry breaking induces coupling and loss difference between the eigenstates of the two bands at $k = 0$, leading to the EPs and OAM gaps. The EPs induce bifurcations of the imaginary parts of the eigenfrequencies, and the OAM gap enables selective transmission of one eigenstate. These together give rise to the enhanced acoustic HD in comparison with that of the C_4 system.

V. C_2 LATTICE WITH HOMOGENEOUS LOSS

In the C_2 lattice system in Fig. 3, the symmetry breaking is induced by the inhomogeneous loss in the resonator, i.e., the loss is only added to two opposing sections of the resonator. To further understand the effect of the rotation symmetry, we consider another type of C_2 system shown in Fig. 7(a), where the loss is homogeneously added to the whole resonator, and the geometry of the resonator has a C_2 rotation symmetry since we set internal blades $r_1 \neq r_2$. Figures 7(b) and 7(c) show the imaginary and real parts of the complex band structure of this system, respectively. We notice that this system does not give rise to EPs. Because of the C_2 symmetry, the chiral dipole bands have two OAM gaps, as indicated by the blue and red ribbons in Fig. 7(c). Figure 7(d) shows the transmission and reflection of opposite helical sounds for loss $\alpha = 0.02$. As seen, in the frequency range of the polarization gaps (denoted by blue and red ribbons), the differential reflection and differential transmission reach the maximums. Figure 7(e) shows the absorption of opposite helical sounds as a function of loss strength α. Similar to the previous cases, the acoustic HD first increases and then decreases with a maximum at about $\alpha = 0.02$. Figure 7(f) shows the absorptions of opposite helical sounds, where the frequency ranges marked by the blue
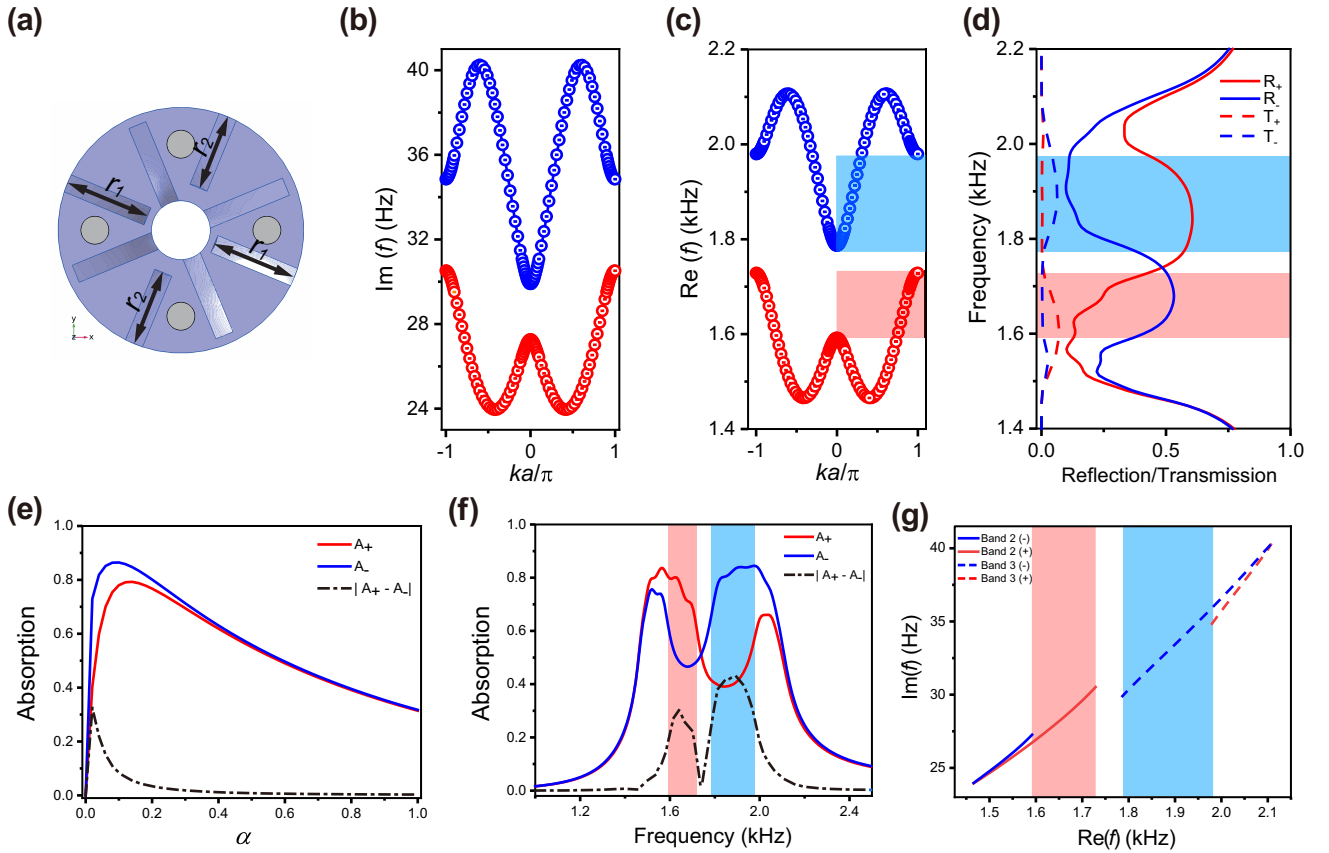
FIG. 7. (a) The unit cell with a geometry satisfying C_2 rotation symmetry. The lengths of the outer blades are not equal: $r_1 \neq r_2$ ($r_1 = 1.76$ cm, $r_2 = 1.56$ cm). (b) The real part and (c) the imaginary part of the complex band structure. (d) The transmission and reflection of helical sounds carrying opposite OAM. We considered the 1D lattice with ten unit cells and $\alpha = 0.02$. (e) The absorption of opposite helical sounds as a function of loss parameter α. (f) The absorption of opposite helical sounds corresponding to the case of (d). (g) The complex eigenfrequencies of the two dipole bands plotted in the complex plane. The red and blue ribbons in (d), (f), and (g) denote the OAM band gaps.

and red ribbons correspond to that in Figs. 7(c) and 7(d). As expected, the maximum acoustic HD appears within the two frequency ranges corresponding to the two OAM gaps. For completeness, we also plot the eigenfrequencies of the dipole bands in the complex plane, as shown in Fig. 7(g). Similar to the case in Fig. 6(c), at the same value of Re(f), the value of Im(f) for the eigenstates with opposite OAM are different, indicating different losses of the two states. However, the difference of Im(f) for the same Re(f) near the boundaries of the OAM gaps is smaller compared with the case in Fig. 6(c), due to the absence of the EPs-induced bifurcations. These results confirm the important effect of structural symmetry on the absorption of helical sounds.

VI. DISCUSSION AND CONCLUSION

In optical systems, strong HD can appear even if the materials of chiral structures contain homogeneous loss. This is because the chiral structures break inversion symmetry and the induced optical fields are in general different for incident helical lights carrying opposite OAM. Since the absorption strongly depends on the distribution of the fields, HD naturally appears in such chiral structures. Our results in this paper uncover a nontrivial counterpart of optical HD in acoustics. In contrast to the optical HD, the acoustic HD can be very weak

in chiral structures with homogeneous material loss. Without the coupling between the opposite chiral dipoles induced in the structures, the absorption of incident helical sounds with opposite OAM is similar. To enhance the HD, one can induce the coupling between opposite chiral dipoles by breaking the C_4 rotation symmetry. In our system, this symmetry breaking is realized by selectively adding material loss to the chiral resonators or engineering the resonators' geometry. The first approach also benefits from the interesting physics of non-Hermitian EPs, where the bifurcation of complex band structures in the symmetry-breaking phase can also enhance the acoustic HD. We emphasize that although a periodic lattice of the chiral resonators is considered in this study, the acoustic HD can also happen to a single chiral resonator, except that the differential absorption will be smaller. We have applied complex band structures and effective Hamiltonians in k space to explain the observed phenomena. For a single chiral resonator, such explanations are not applicable since the resonator represents an open scattering system. In this case, a microscopic picture based on multipole expansions may be employed to understand its absorption properties, and the associated physics remains to be explored. Experimental demonstration of the proposed acoustic HD is possible. The chiral resonators can be fabricated by using three-dimensional printing and then assembled into a 1D lattice. Inhomogeneous

loss can be introduced into the lattice by adding absorbing materials (e.g., foams) to the selected domains of the chiral resonators [i.e., the blue regions in the insets of Figs. 2(b) and Fig. 3(a)]. The incident helical sounds can be generated by using four speakers that couple to the four tubes of the resonator. The absorption can be determined from the measured transmission and reflection of the structure.

In conclusion, we proposed a chiral lattice structure that can selectively absorb helical sounds with opposite OAM. The phenomenon represents the acoustic counterpart of optical HD effect. We have shown that this acoustic HD strongly depends on the rotation symmetry of the lattice. The structure with C_2 symmetry can give rise to a much larger HD compared to the structure with C_4 symmetry. This enhancement is attributed to the OAM gaps and non-Hermitian EPs induced by the coupling of opposite chiral dipole modes of the resonators. The results pave the way for further investigations of chiral sound-matter interactions in artificial structures and metamaterials. The proposed structures can also find important applications in manipulations of acoustic OAM.

[1] V. K. Valev, J. J. Baumberg, C. Sibilia, and T. Verbiest, Chirality and chiroptical effects in plasmonic nanostructures: Fundamentals, recent progress, and outlook, Adv. Mater. **25**, 2517 (2013).

[2] S. B. Wang and C. T. Chan, Lateral optical force on chiral particles near a surface, Nat. Commun. **5**, 3307 (2014).

[3] W. Ye, X. Yuan, C. Guo, J. Zhang, B. Yang, and S. Zhang, Large Chiroptical Effects in Planar Chiral Metamaterials, Phys. Rev. Appl. **7**, 054003 (2017).

[4] M. Hentschel, M. Schäferling, X. Duan, H. Giessen, and N. Liu, Chiral plasmonics, Sci. Adv. **3**, e1602735 (2017).

[5] J. Mun, M. Kim, Y. Yang, T. Badloe, J. Ni, Y. Chen, C.-W. Qiu, and J. Rho, Electromagnetic chirality: From fundamentals to nontraditional chiroptical phenomena, Light Sci. Appl. **9**, 139 (2020).

[6] N. Berova, K. Nakanishi, and R. W. Woody, *Circular Dichroism: Principles and Applications* (Wiley, New York, 2000)

[7] N. J. Greenfield, Using circular dichroism spectra to estimate protein secondary structure, Nat. Protoc. **1**, 2876 (2006).

[8] R. H. Garrett and C. M. Grisham, *Biochemistry* (Cengage Learning, Boston, 2012).

[9] K. Binnemans, Ionic Liquid Crystals, Chem. Rev. **105**, 4148 (2005).

[10] A. V. Rogacheva, V. A. Fedotov, A. S. Schwanecke, and N. I. Zheludev, Giant Gyrotropy due to Electromagnetic-Field Coupling in a Bilayered Chiral Structure, Phys. Rev. Lett. **97**, 177401 (2006).

[11] M. Decker, M. W. Klein, M. Wegener, and S. Linden, Circular dichroism of planar chiral magnetic metamaterials, Opt. Lett. **32**, 856 (2007).

[12] S. Zhang, Y.-S. Park, J. Li, X. Lu, W. Zhang, and X. Zhang, Negative Refractive Index in Chiral Metamaterials, Phys. Rev. Lett. **102**, 023901 (2009).

[13] M. Decker, M. Ruther, C. E. Kriegler, J. Zhou, C. M. Soukoulis, S. Linden, and M. Wegener, Strong optical activity from twisted-cross photonic metamaterials, Opt. Lett. **34**, 2501 (2009).

[14] R. Zhao, T. Koschny, E. N. Economou, and C. M. Soukoulis, Comparison of chiral metamaterial designs for repulsive Casimir force, Phys. Rev. B **81**, 235126 (2010).

[15] T.-T. Kim, S. S. Oh, H.-S. Park, R. Zhao, S.-H. Kim, W. Choi, B. Min, and O. Hess, Optical activity enhanced by strong inter-molecular coupling in planar chiral metamaterials, Sci. Rep. **4**, 5864 (2014).

[16] M. Saba, M. Thiel, M. D. Turner, S. T. Hyde, M. Gu, K. Grosse-Brauckmann, D. N. Neshev, K. Mecke, and G. E. Schröder-Turk, Circular Dichroism in Biological Photonic Crystals and Cubic Chiral Nets, Phys. Rev. Lett. **106**, 103902 (2011).

[17] S. S. Oh, A. Demetriadou, S. Wuestner, and O. Hess, On the origin of chirality in nanoplasmonic gyroid metamaterials, Adv. Mater. **25**, 612 (2013).

[18] J. A. Dolan, B. D. Wilts, S. Vignolini, J. J. Baumberg, U. Steiner, and T. D. Wilkinson, Optical properties of gyroid structured materials: From photonic crystals to metamaterials, Adv. Opt. Mater. **3**, 12 (2015).

[19] S. Jia, J. Peng, Y. Cheng, and S. Wang, Chiral discrimination by polarization singularities of single metal sphere, arXiv:2108.00286.

[20] M. Schäferling, *Chiral Nanophotonics: Chiral Optical Properties of Plasmonic Systems* (Springer, Cham, 2017).

[21] K. A. Forbes and D. L. Andrews, Orbital angular momentum of twisted light: Chirality and optical activity, J. Phys. Photonics **3**, 022007 (2021).

[22] M. Babiker, C. R. Bennett, D. L. Andrews, and L. Davila Romero, Orbital Angular Momentum Exchange in the Interaction of Twisted Light with Molecules, Phys. Rev. Lett. **89**, 143601 (2002).

[23] T. Wu, R. Wang, and X. Zhang, Plasmon-induced strong interaction between chiral molecules and orbital angular momentum of light, Sci. Rep. **5**, 18003 (2015).

[24] S. Wang, Z.-L. Deng, Y. Cao, D. Hu, Y. Xu, B. Cai, L. Jin, Y. Bao, X. Wang, and X. Li, Angular momentum-dependent transmission of circularly polarized vortex beams through a plasmonic coaxial nanoring, IEEE Photonics J. **10**, 1 (2018).

[25] K. A. Forbes and D. L. Andrews, Optical orbital angular momentum: Twisted light and chirality, Opt. Lett. **43**, 435 (2018).

[26] W. Brullot, M. K. Vanbel, T. Swusten, and T. Verbiest, Resolving enantiomers using the optical angular momentum of twisted light, Sci. Adv. **2**, e1501349 (2016).

[27] J. Ni, S. Liu, G. Hu, Y. Hu, Z. Lao, J. Li, Q. Zhang, D. Wu, S. Dong, J. Chu, and C.-W. Qiu, Giant helical dichroism of single chiral nanostructures with photonic orbital angular momentum, ACS Nano **15**, 2893 (2021).

[28] K. Y. Bliokh and F. Nori, Spin and orbital angular momenta of acoustic beams, Phys. Rev. B **99**, 174310 (2019).

[29] S. Wang, G. Zhang, X. Wang, Q. Tong, J. Li, and G. Ma, Spin-orbit interactions of transverse sound, Nat. Commun. **12**, 6125 (2021).

[30] J. Lu, C. Qiu, M. Ke, and Z. Liu, Valley Vortex States in Sonic Crystals, Phys. Rev. Lett. **116**, 093901 (2016).

[31] X. Jiang, Y. Li, B. Liang, J. C. Cheng, and L. Zhang, Convert Acoustic Resonances to Orbital Angular Momentum, Phys. Rev. Lett. **117**, 034301 (2016).

[32] H. Esfahlani, H. Lissek, and J. R. Mosig, Generation of acoustic helical wavefronts using metasurfaces, Phys. Rev. B **95**, 024312 (2017).

[33] J. Liu, B. Liang, J. Yang, and J. Cheng, Generation of Non-aliased two-dimensional acoustic vortex with enclosed metasurface, Sci. Rep. **10**, 3827 (2020).

[34] S.-W. Fan, Y.-F. Wang, L. Cao, Y. Zhu, A.-L. Chen, B. Vincent, B. Assouar, and Y.-S. Wang, Acoustic vortices with high-order orbital angular momentum by a continuously tunable metasurface, Appl. Phys. Lett. **116**, 163504 (2020).

[35] Y. Fu, C. Shen, X. Zhu, J. Li, Y. Liu, S. A. Cummer, and Y. Xu, Sound vortex diffraction via topological charge in phase gradient metagratings, Sci. Adv. **6**, eaba9876 (2020).

[36] Z. Zou, R. Lirette, and L. Zhang, Orbital Angular Momentum Reversal and Asymmetry in Acoustic Vortex Beam Reflection, Phys. Rev. Lett. **125**, 074301 (2020).

[37] C. E. M. Demore, Z. Yang, A. Volovick, S. Cochran, M. P. MacDonald, and G. C. Spalding, Mechanical Evidence of the Orbital Angular Momentum to Energy Ratio of Vortex Beams, Phys. Rev. Lett. **108**, 194301 (2012).

[38] D. Baresch, J.-L. Thomas, and R. Marchiano, Observation of a Single-Beam Gradient Force Acoustical Trap for Elastic Particles: Acoustical Tweezers, Phys. Rev. Lett. **116**, 024301 (2016).

[39] C. Shi, M. Dubois, Y. Wang, and X. Zhang, High-speed acoustic communication by multiplexing orbital angular momentum, Proc. Natl. Acad. Sci. USA **114**, 7250 (2017).

[40] S. Wang, G. Ma, and C. T. Chan, Topological transport of sound mediated by spin-redirection geometric phase, Sci. Adv. **4**, eaaq1475 (2018).

[41] W. Wang, Y. Tan, B. Liang, G. Ma, S. Wang, and J. Cheng, Generalized momentum conservation and Fedorov-Imbert linear shift of acoustic vortex beams at a metasurface, Phys. Rev. B **104**, 174301 (2021).

[42] www.comsol.com.

[43] X.-L. Zhang, S. Wang, W.-J. Chen, and C. T. Chan, Exceptional points and symmetry recovery in a two-state system, Phys. Rev. A **96**, 022112 (2017).

[44] X.-L. Zhang, S. Wang, B. Hou, and C. T. Chan, Dynamically Encircling Exceptional Points: *In situ* Control of Encircling Loops and the Role of the Starting Point, Phys. Rev. X **8**, 021066 (2018).

[45] B. Zhen, C. W. Hsu, Y. Igarashi, L. Lu, I. Kaminer, A. Pick, S. L. Chua, J. D. Joannopoulos, and M. Soljačić, Spawning rings of exceptional points out of Dirac cones, Nature (London) **525**, 354 (2015).

[46] C. Wu, H. Li, Z. Wei, X. Yu, and C. T. Chan, Theory and Experimental Realization of Negative Refraction in a Metallic Helix Array, Phys. Rev. Lett. **105**, 247401 (2010).

[47] M. A. Miri and A. Alù, Exceptional points in optics and photonics, Science **363**, eaar7709 (2019).

[48] J. Wiersig, Review of exceptional point-based sensors, Photon. Res. **8**, 1457 (2020).

[49] L. Luo, Y. Shao, J. Li, R. Fan, R. Peng, M. Wang, J. Luo, and Y. Lai, Non-hermitian effective medium theory and complex dirac-like cones, Opt. Express **29**, 14345 (2021).